INTERNATIONAL JOURNAL FOR NUMERICAL METHODS IN FLUIDS, VOL. 10, 827–848 (1990)

GLOBAL PRESSURE RELAXATION FOR LAMINAR TWO-DIMENSIONAL INTERNAL FLOW

D. ROSENBAUM* AND S. G. RUBIN

Department of Aerospace Engineering and Engineering Mechanics, ML 70, University of Cincinnati, Cincinnati, OH 45221, U.S.A.

SUMMARY

This study extends the reduced Navier–Stokes (RNS) global pressure relaxation procedure developed by Rubin and co-workers for external flow to internal flow applications. The streamwise pressure gradient is split into a backward-differenced or initial value component, as in boundary layer marching, and a forward-differenced or boundary value component that represents the elliptic downstream effects. The streamwise convection terms are upwind-differenced and all other streamwise derivatives are backward-differenced. We thus obtain a standard boundary layer marching technique imbedded in a conventional line relaxation technique. For compressible flow the pressure iteration determines the interior flow interation as well as the inlet mass flux that is consistent with the outflow pressure boundary condition. Results have been computed for incompressible flow in both rectangular and curved channels, and for subsonic compressible flow in the simulation of an aerofoil in a wind tunnel. Converged solutions were obtained over a range of Reynolds numbers generating small to moderately large separation bubbles.

KEY WORDS Reduced Navier–Stokes Strong interaction Global pressure relaxation Two-dimensional Laminar Internal flow

INTRODUCTION

The difficulties inherent in obtaining large-Reynolds-number (Re) Navier–Stokes (NS) solutions for strong interaction flow problems have led to the development of approximate forms of these equations. These are applicable to particular flow regimes and are more computationally efficient. The earliest of these approximations include inviscid potential and Euler theories and Prandtl viscous boundary layer theory.[1] Classical matched inviscid-outer/viscous-inner (boundary layer) solution procedures were in turn extended with higher-order boundary layer (HOBL) theory,[2] interacting boundary layer (IBL) theory[3] and triple-deck theory.[4]

The most advantageous feature of the boundary layer model is that the resulting system of equations is initial value in character (mathematically parabolic) and can be solved numerically by simple marching procedures. This concept of 'boundary layer' marching technique was extended to more complete systems of equations with the parabolized Navier–Stokes (PNS) formulation. For this approximation all terms of both the Euler and Second-order boundary layer equations were retained within a single equation set and solved as an initial value problem. However, as is now known, the inclusion of the coupled streamwise pressure gradient p_x leads to an ill-posed initial value problem, and exponentially growing 'departure' solutions result. The

* Senior Engineer, Garrett Turbine Eigine Company, Phoenix, AZ, U.S.A.

0271–2091/90/070827–22$11.00

Received 26 October 1988
Revised 3 October 1989

variable streamwise pressure gradient in PNS or interacting boundary layer theory introduces an elliptic upstream interaction between the boundary layer and inviscid flow.

In order to suppress the ellipticity and permit parabolic marching for weakly intereacting flows, different treatments were applied for the p_x term. It was neglected for hypersonic flow[5] and calculated only in supersonic regions for large-Mach-number supersonic viscous flow,[6] i.e. sublayer approximation. These procedures are not useful for accurate subsonic flow computation where upstream influences will be significant. From characteristic analysis[7] it was shown that the streamwise pressure gradient should be split into an initial value part 'ωp_x' and a boundary value part '$(1-\omega)p_x$', where for constant stagnation enthalpy, ω is defined by the condition

$$\omega < \frac{\gamma M_x^2}{1+(\gamma-1)M_x^2} \qquad \left(M_x \triangleq \frac{u}{a}\right).$$

Only the 'ωp_x' term is retained for the initial value PNS calculations. More recently, Rubin[8] has shown that the flux pressure decomposition can be obtained directly with a new form of flux vector splitting that correlates contributions from positive and negative flux eigenvalues.

The original initial value PNS model, although providing a simpler solution technique for boundary-layer-like flows, was not satisfactory since the elliptic viscous–inviscid interaction effects were simply suppressed rather than calculated. The restoration of the complete streamwise pressure gradient as an unknown leads to what is termed reduced Navier–Stokes (RNS) theory. This permits simulation of elliptic effects due to viscous–inviscid interaction, as well as the elliptic acoustic pressure propagation of inviscid subsonic flow. In order to formulate a numerical method that could preserve the entire streamwise pressure gradient, the differencing of the p_x term was further explored in Reference 9. In this study (for incompressible flow where $\omega \triangleq 0$) it was shown that stable marching could be achieved with 'forward' differencing for p_x given by

$$p_x = \frac{p_{i+1,j} - p_{i,j}}{\Delta x_i}$$

where i is the grid index in the streamwise (x) co-ordinate and j is the index in the normal (y) co-ordinate. Convective streamwise derivatives were upwind-differenced. All flow variables were coupled at the streamwise location i and the solution was marched from an initial station downstream. The downstream pressure value $p_{i+1,j}$ was relaxed from some initial guess or inviscid solution. Upon completion of the one sweep, the new values of $p_{i+1,j}$ were used for the next sweep. This method provided for a multisweep pressure relaxation process similar to the IBL method. Unlike the IBL method, however, this interation is simulated with a single set of equations valid throughout the entire flow field.

Applications of the forward-differencing procedure were presented in References 10–14. The compressible flux-split analysis with backward differencing for the component ωp_x and forward-differencing for $(1-\omega)p_x$ was verified by numerical solutions in References 15 and 16. The RNS system contains all terms of the Euler, second-order boundary layer, IBL and triple-deck theories in a single set of equations. The RNS model, like the IBL and triple-deck equations, provides an approximation of the full NS equations which is capable of calculating strong viscous–inviscid interactions. This system also allows for the evaluation of upstream influence due to inviscid acoustic pressure propagation. The free pressure interaction permits a sigularity-free calculation through regions of separated flow.

In the present study the RNS global pressure relaxation procedure, which has been utilized in the past primarily for external flow, is extended to internal flow applications. Problems are considered for both incompressible and subsonic compressible flow. Incompressible flow cases include unseparated flow in rectangular channels and moderate-to-large separated flow in curved

channels, for which comparison solutions are available in the literature. For compressible flow, solutions are obtained for flow past a NACA0012 aerofoil in a variable diameter wind tunnel and over a range of Mach number and Reynolds number. The Reynolds number range considered for the compressible flow cases includes flows with significant regions of recirculation.

GOVERNING EQUATIONS

The RNS equations are obtained by retaining all terms in the NS equations which appear, to second order, in both the inner expansion (boundary layer) and outer expansion (inviscid region) of HOBL theory. These equations are expressed in an appropriate 'streamline' or body-fitted co-ordinate system. The resulting RNS equations for orthogonal curvilinear co-ordinates in non-dimensional form are:

continuity

$$\frac{\partial}{\partial t}(h_1 h_2 h_3 \rho) + \frac{\partial}{\partial \xi}(h_2 h_3 \rho u) + \frac{\partial}{\partial \eta}(h_1 h_3 \rho v) = 0, \tag{1}$$

ξ-momentum

$$\frac{\partial}{\partial t}(\rho u h_1 h_2 h_3) + [\rho u^2 h_2 h_3]_\xi + [\rho v u h_1 h_3]_\eta + [\rho v u h_{1_\eta} h_3] - [\rho v^2 h_{2_\xi} h_3]$$
$$= \varepsilon^2 \left\{ \left[\frac{h_1}{h_2} \left(\frac{u}{h_1} \right)_\eta h_1 h_3 \right]_\eta + \left[\frac{h_1}{h_2} \left(\frac{u}{h_1} \right)_\eta h_{1_\eta} h_3 \right] \right\} - p_\xi h_2 h_3, \tag{2}$$

η-momentum

$$\frac{\partial}{\partial t}(\rho v h_1 h_2 h_3) + [\rho u v h_2 h_3]_\xi + [\rho v^2 h_1 h_3]_\eta - [\rho u^2 h_{1_\eta} h_3] + [\rho u v h_{2_\xi} h_3]$$
$$= - p_\eta h_1 h_3, \tag{3}$$

stagnation enthalpy energy equation

$$\frac{\partial}{\partial t}(\rho H h_1 h_2 h_3) - E_r \frac{\partial}{\partial t}(p h_1 h_2 h_3) + \frac{\partial}{\partial \xi}(\rho H u h_2 h_3)$$
$$+ \frac{\partial}{\partial \eta} \left(\left\{ \rho H v - \varepsilon^2 \left[\frac{\mu}{Pr h_2} \frac{\partial H}{\partial \eta} + E_r \mu \left(1 - \frac{1}{Pr} \right) \frac{1}{h_2} \frac{\partial}{\partial \eta} \left(\frac{u^2}{2} \right) \right. \right. \right.$$
$$\left. \left. \left. - E_r \mu \frac{u^2}{h_1 h_2} \frac{\partial h_1}{\partial \eta} \right] \right\} h_1 h_3 \right) = 0, \tag{4}$$

equation of state

$$p = \frac{\gamma_r - 1}{\gamma_r E_r} \left[\rho \left(H - \frac{E_r}{2}(u^2 + v^2) \right) - \left(1 - \frac{E_r}{2} \right) \right], \tag{5}$$

where

$$\varepsilon \triangleq \frac{1}{(Re)}, \qquad Re \triangleq \frac{\rho_r u_r L_r}{\mu_r}, \qquad E_r \triangleq \frac{u_r^2}{H_r} \quad \text{(reference Eckert number).}$$

The subscript 'r' denotes reference value, h_1, h_2, h_3 are metric scale factors, u and v are the contravariant physical velocity components in the streamwise (ξ) and normal (η) co-ordinate directions, ρ is density, p is pressure, γ_r is the reference specific heat ratio, and the stagnation (or total) enthalpy H is defined (in non-dimensional form) as

$$H = \left(1 - \frac{E_r}{2}\right)T + \frac{E_r}{2}(u^2 + v^2). \tag{6}$$

The reference Eckert number E_r is related to a reference Mach number M_r by the relation

$$E_r = \frac{(\gamma_r - 1)M_r^2}{1 + [(\gamma_r - 1)/2]M_r^2}. \tag{7}$$

We note that the RNS equations do not contain viscous streamwise diffusion terms in the streamwise momentum equation or any viscous diffusion terms in the normal momentum equation. The normal direction pressure gradient term $h_1 h_3 p_\eta$ as well as the longitudianl curvature term $-\rho u^2 h_{1_\eta} h_3$ are completely retained. Furthermore, all terms in the inviscid Euler equations, i.e. all convection terms and pressure gradients, including the streamwise pressure gradient p_ξ are retained.

For compressible flow the pressure p is expressed at each streamwise marching location ξ_i in terms of ρ, u, v and H with the equation of state (5). For incompressible flow $\rho \triangleq 1$ in equations (1)–(4). For the present analysis μ, c_p and Pr (dynamic viscosity coefficient, specific heat at constant pressure, and Prandtl number) are all treated as constants. We note that for $Pr = 1$, steady flow, an inlet boundary condition $H = H^*/H_r = 1$ (where $(\ )^*$ denotes a dimensional quantity) and an adiabatic wall boundary condition $\partial H/\partial\eta|_{\text{wall}} = 0$, the assumed solution

$$H(\xi, \eta) \triangleq 1 \tag{8}$$

satisfies equation (4) to within an error associated with second-order curvature terms. For the present analysis, in order to expedite numerical solution, equation (8) is used for H. The full equation (4) is,. however, included in the program and was tested for unseparated flows. The results show little change from the constant H solutions.

Review and treatment of interaction terms in the RNS equations

The essential terms in the RNS system that capture the upstream influence and strong viscous–inviscid interaction are the streamwise pressure gradient term $h_2 h_3 p_\xi$, the streamwise v-convection term $(\rho u v h_2 h_3)_\xi$ and the normal pressure gradient term $h_1 h_3 p_\eta$. The coupled solution of the full RNS equations, including these terms, is the feature that enables the simulation of the elliptic interaction.

From previous analyses[7, 8, 17–19] it has been shown that the upstream influence is properly represented if the pressure gradient p_ξ is represented by a form of flux vector splitting given by

$$p_\xi = \omega_v \vec{p}_\xi + (1 - \omega_v)\overleftarrow{p}_\xi, \tag{9}$$

where $\omega_v \vec{p}_\xi$ is backward-differenced and $(1 - \omega_v)\overleftarrow{p}_\xi$ is forward-differenced. The latter term becomes part of a multisweep global line relaxation method. The differenced form of (9) is given as

$$p_\xi = \omega_v \frac{p^n_{1,j} - p^n_{i-1,j}}{\Delta\xi_i} + (1 - \omega_v)\frac{p^{n-1}_{i+1,j} - p^n_{i,j}}{\Delta\xi_{i+1}} \tag{10}$$

(where i is the grid index in the streamwise (ξ) co-ordinate and j is the index in the normal (η) co-ordinate) or, alternatively, an averaged form spread over three points in the η-direction. This was

used in the compressible flow version of the code. The switch function ω_v (for H-constant)[8] becomes

$$\omega_v = \sigma_v \min\left\{\frac{\gamma_r M_\xi^2}{1+(\gamma_r-1)M_\xi^2}, 1\right\} \tag{11}$$

and

$$\sigma_v = \text{constant} \quad (0 \le \sigma_v \le 1),$$

$$M_\xi \triangleq M_r \frac{u}{\sqrt{T}},$$

where M_ξ is the streamwise component of the local Mach number and T is temperature. The constant factor σ_v is an experimentally determined 'damping factor' which is taken to be less than or equal to one; σ_v is taken as 1·0 for most applications.

For internal flow a second stability or stiffness effect was encountered. This was not previously found for external flow RNS calculations. For each marching sweep a non-physical spatial oscillation associated with the streamwise pressure gradient p_ξ was encountered. The source of this behaviour was traced to the presence of the $(\rho uvh_2h_3)_\xi$ interaction term in the normal momentum equation and appeared to be directly associated with the additional mass conservation constraint. This adds considerable stiffness to the system and requires some additional damping during the transient stages of the computation. The influence of this term was suppressed in the transient by overrelaxing the p_η term. This is equivalent to adding a fictitious $p_{\eta t}$ term. It was found that the oscilliations were suppressed for an overrelaxation factor $\omega \gtrsim 10$. Global convergence was then assured.

For compressible flow the presence of the backward-differenced or initial value portion of p_ξ requires an inflow boundary condition on p. For subsonic flow the downstream 'back' pressure should completely determine the inlet mass flow. Therefore the inlet pressure boundary condition is computed by a derivative pressure condition. For simplicity, a second derivative condition was selected. This allows the inlet pressure and hence the inlet mass flow to be determined as part of the solution.

INCOMPRESSIBLE FLOW FORMULATION AND BOUNDARY CONDITIONS

For incompressible flow the RNS equations are solved for semi-infinite rectangular channels and doubly infinite channels. These are formed by two streamlines of the potential flow past a cylinder. The solution region is always rectangular in the curvilinear computational plane, so that $\xi_1 \le \xi \le \xi_m$, $\eta_1 = 0 \le \eta \le \eta_m$. For incompressible flow, $M_\xi \to 0$ so that $\omega_v \to 0$ in (9) or (10). The pressure gradient p_ξ is fully elliptic and therefore an inflow boundary condition for pressure is not required.

As the channel walls become straight and parallel downstream, the co-ordinate transformation asymptotes to $\xi = x$, $\eta = y$, $h_1 = h_2 = h_3 = 1{\cdot}0$. The downstream boundary is prescribed far downstream in the straight wall region so that fully developed flow conditions are achieved. Reference 20 delineates three regions of incompressible flow development in rectangular channels. The first is a small leading edge region of order $x = O(Re^{-1})$ within which the complete Navier–Stokes equations are required to model the flow. The latter two regions, in which the RNS model is applicable, are measured relative to the development length co-ordinate ζ given by

$$\zeta \triangleq \beta \sqrt{\left(\frac{2x_{h/2}}{Re_{h/2}}\right)} \qquad (\beta = 1{\cdot}216\,78), \tag{12}$$

with x and Re based on the half-channel height $h^*/2$. The first of these is an entry flow region of length $\zeta = O(1)$ wherein the flow structure consists of a potential core and boundary layers along the walls. Beyond $\zeta = 0{\cdot}2$ the boundary layers increase to the point where they fill a significant fraction of the duct. Eventually the boundary layers merge for $\zeta = O(1)$ to form a fully viscous region. In the fully viscous region, $p_y = 0$ to second order and no further viscous–inviscid interaction occurs. Finally, for $\zeta = \zeta_{ent} \gg 1$, fully developed conditions are achieved. The length ζ_{ent} is termed the channel 'entrance length'.

In the fully developed (Poiseuille) flow region we have

$$u = u(y), \qquad v \triangleq 0, \qquad p = p(x), \qquad \frac{dp}{dx} = \text{constant}. \tag{13}$$

Applying equations (13) to governing equations (1)–(3) (for $\xi = x$, $\eta = y$, $h_1 = h_2 = h_3 = 1{\cdot}0$) and utilizing no-slip boundary conditions we obtain the classical parabolic Poiseuille profile for which the pressure gradient $p_\xi \triangleq p_{fd,\xi}$ is purely a function of Re and mass flow rate m.

To accomodate the non-vanishing nature of the downstream pressure gradient and the developing flow character of the incompressible internal flow problem, it is convenient to assume the following pressure decomposition for the incompressible code development:

$$p(\xi, \eta) = p_0(\xi) + p'(\xi, \eta) \triangleq \bar{p}_{uw}(\xi) + p'(\xi, \eta), \tag{14}$$

$$\triangleq p_{fd}(\xi) + p_{uw}(\xi) + p'(\xi, \eta), \tag{15}$$

where for convenience $p_0(\xi)$ is identified with the value of pressure on the upper wall, $\bar{p}_{uw}(\xi)$; this portion is further split[21] into a fully developed flow component $p_{fd}(\xi)$ and a perturbation $p_{uw}(\xi)$. Since only gradients of p occur in the equations, the value $p_{fd,\xi}$ can be added *a priori* in equation (3). The remaining $dp_{uw}/d\xi$ and $\partial p'/\partial \xi$ derivatives involve differences of perturbation pressures that tend to zero as $\zeta \to \zeta_{ent}$. Setting $p' = 0$ for $0 \leq \eta \leq \eta_m$ at the exit boundary is somewhat constraining and therefore $p'_\xi = 0$ is used as a less restrictive exit boundary condition.

The variable p' is coupled to the normal momentum equation and contains the elliptic acoustic interaction. The value of p' is zero on the top wall and the component p_{uw,ξ_i} is determined at each marching location ξ_i by a Newton method iteration to enforce the boundary condition $v = 0$ on the top wall. Alternatively, use of a general matrix inversion algorithm (see compressible flow discussion in numerical scheme section) obviates the need for the p_{uw}/p' pressure splitting. The downstream pressure boundary condition then becomes

$$\tilde{p}_\xi \to 0 \quad \text{as} \quad \xi \to \xi(\zeta_{ent})$$

where

$$\tilde{p}(\xi, \eta) \triangleq p(\xi, \eta) - p_{fd}(\xi).$$

This is more restrictive since the exit boundary must now be located in the fully developed region and not merely in the fully viscous region.

COMPRESSIBLE FLOW BOUNDARY CONDITIONS AND REFERENCE CONDITIONS

For compressible flow it is no longer numerically convenient to split the pressure, equation (14), since pressure is now related to density and velocity through the equation of state (5). Furthermore, for subsonic flow the downstream static pressure and upstream stagnation conditions completely determine the mass flow through the duct. Thus the pressure, rather than the pressure gradient as applied for fully developed incompressible flow, is prescribed downstream. Once

again, ξ_m is chosen far enough downstream of any disturbance or curved wall region so that the exit station lies in the fully viscous region and the back pressure may be taken as constant.

For numerical convenience we use design, rather than analysis, boundary conditions. In the design boundary condition prescription we assume that the downstream back pressure has already been adjusted to produce the desired inlet Mach number. The inlet Mach number then replaces the stagnation pressure as one of our upstream boundary conditions. The upstream stagnation enthalpy H^* is for perfect gas flow $H^* = H^*(T_0^*)$ (where T_0^* is total temperature) and is specified. The downstream static pressure is non-dimensionalized with respect to back pressure, so that

$$p_r \triangleq p^*_{back} = p^*(\xi_m, \eta) = p^*_m = \text{constant}, \tag{16}$$

$$p(\xi_m, \eta) \triangleq \frac{p^*(\xi_m, \eta) - p_r}{\rho_r u_r^2} = \frac{p^*_m - p_r}{\rho_r u_r^2} = 0 = p_{back}. \tag{17}$$

The reference Mach number M_r is taken to be the inlet Mach number at the centreline of the symmetric duct ($\eta = 0$), where $v = 0$.

As discussed previously, the inlet pressure boundary condition is obtained by equating the upstream and downstream pressure fluxes to give the gradient condition

$$\frac{p^n_{2,j} - p^n_{1,j}}{\Delta\xi_2} = \frac{p^{n-1}_{3,j} - p^n_{2,j}}{\Delta\xi_3}, \tag{18}$$

where n denotes the index of the current global iteration (march). Equation (18) is tantamount to extrapolating the inlet value $p_{1,j}$ from downstream values and is equivalent to the $p_{\xi\xi} = 0$ inlet boundary condition used in Reference 22. Equation (18) provides the inlet static pressure.

The non-dimensional incompressible and compressible flow boundary conditions are summarized as follows:

inflow boundary

$\xi = \xi_1$: $u = u_1(\eta)$,
$v = v_1(\eta)$ (when $v_1(\eta)$ is known),
or else
$v_\xi = 0$,
$H = 1$ (compressible flow),
$p_{\xi\xi} = 0$ (compressible flow);

centreline boundary

$\eta = 0$: $u_\eta = 0$,
$H_\eta = 0$ (compressible flow),
$v = 0$,
$u(-\eta) = +u(\eta)$, $H(-\eta) = +H(\eta)$, $v(-\eta) = -v(\eta)$;

wall boundary

$\eta = n_m$ or $\eta = 0$: $u = 0$,
$H_\eta = 0$ (adiabatic wall),
$v = 0$;

outflow boundary

$\xi = \xi_m$: $p'_\xi = 0$ (incompressible flow),
$p = 0$ (compressible flow).

Symmetry boundary conditions are used in evaluating the ξ-momentum and energy equations on the wind tunnel centreline.

The $v_\xi = 0$ inlet boundary condition is preferable when the inlet station $\xi = \xi_1$ lies in the entry flow region. The inlet flow then consists of a uniform potential core and boundary layers along the walls. The $v_\xi = 0$ inlet boundary condition enforces irrotationality in the inviscid core and continuity of the displacement thickness slope at the inlet. This boundary condition is also useful when the inlet station is in a first-order boundary layer region upstream of the RNS interaction zone. $v_\xi(\xi_1, \eta) = 0$ enforces the required $p_\eta = 0$ and allows the interaction region, signified by non-zero v_ξ, to develop gradually.

The inlet mass flux iteration is performed iteratively by repeated calculations of the equations at station ξ_2 to a desired tolerance. This requires about three to four local iterations in the early global iterations; a single iteration is necessary as the global process approaches convergence. This iteration process adjusts the mass flux through re-evaluation of the inlet (station 1) density consistent with the inlet pressure given by equation (18).

NUMERICAL SCHEME

The equations are differenced using first-order upwind differences in the ξ-direction and central differences in the η-direction. Allowance is made for unequal spacing in both curvilinear co-ordinates, ξ and η. The difference molecule is shown in Figure 1. The continuity and η-momentum equations are first-order in η and are evaluated using two-point trapezoidal-rule differencing at the half-point $(i, j - \frac{1}{2})$ and the ξ-momentum and energy equations are evaluated at the nodes (i, j). All ξ-derivatives, other than ξ-convection terms, are backward-differenced. All ξ-convection terms are quasi-linearized and upwind-differenced. The energy equation for compressible flow is uncoupled from continuity and ξ- and η-momentum and solved in uncoupled in an outer iteration at each marching station ξ_i.

The upwind ξ-convection derivatives are differenced as follows (actually averaged over points $(i, j-1) \rightarrow (i, j+1)$ for compressible flow):

$$[\rho u^2 h_2 h_3]_\xi = \beta_j \frac{[\rho u^2 h_2 h_3]^k_{i,j} - [\rho u^2 h_2 h_3]^n_{i-1,j}}{\Delta\xi_i} + (1 - \beta_j) \frac{[\rho u^2 h_2 h_3]^{n-1}_{i+1,j} - [\rho u^2 h_2 h_3]^k_{i,j}}{\Delta\xi_{i+1}} \tag{19}$$

with $\beta_j = 1$ for $u^{k-1}_{i,j} > 0$ and $\beta_j = 0$ for $u^{k-1}_{i,j} < 0$ (where k is the index of the local quasi-linearization iteration at station ξ_i in global sweep n). In the vicinity of the change from reverse flow to forward flow, if the downstream value $u^{n-1}_{i+1,j} > 0$ while $u^{k-1}_{i,j}$ is still less than zero, then a modified form of the forward-differencing procedure is used. In this modified scheme, interpolation is used to determine the position where $u^{n-1}_{i+1,j} = 0$. This length is then used for $\Delta\xi_{i+1}$, with $u^{n-1}_{i+1,j}$ set to zero. An analogous procedure is used if $u^n_{i-1,j} < 0$ and $u^k_{i,j}$ has become greater than zero. Values of $u^{n-1}_{i+1,j}$ and $v^{n-1}_{i+1,j}$ from the previous sweep (time level $n-1$) are stored in separation regions.

The finite difference equations at each marching station ξ_i for continuity, ξ-momentum and η-momentum have a block tridiagonal structure. For incompressible flow these equations are solved simultaneously for the dependent variables $u^k_{i,j}$, $v^k_{i,j}$ and $p'^k_{i,j}$, $j = 1, \ldots, j_{\max}$, by a scalar form of the Thomas algorithm. The computer variable $p'_{i,j}$ is the discrete counterpart of the perturbation pressure $p'(\xi, \eta)$ defined in equation (15). The streamwise pressure gradient term becomes

$$(h_2 h_3 p_\xi)_{i,j} = (h_2 h_3)_{i,j} \frac{p'^{n-1}_{i+1,j} - p'^k_{i,j}}{\Delta\xi_{i+1}} + (h_2 h_3)_{i,j} K \left.\frac{d\phi}{d\xi}\right|_{\phi(\xi_i)} + (h_2 h_3)_{i,j} p^k_{\text{uw},\xi_i}, \tag{20}$$

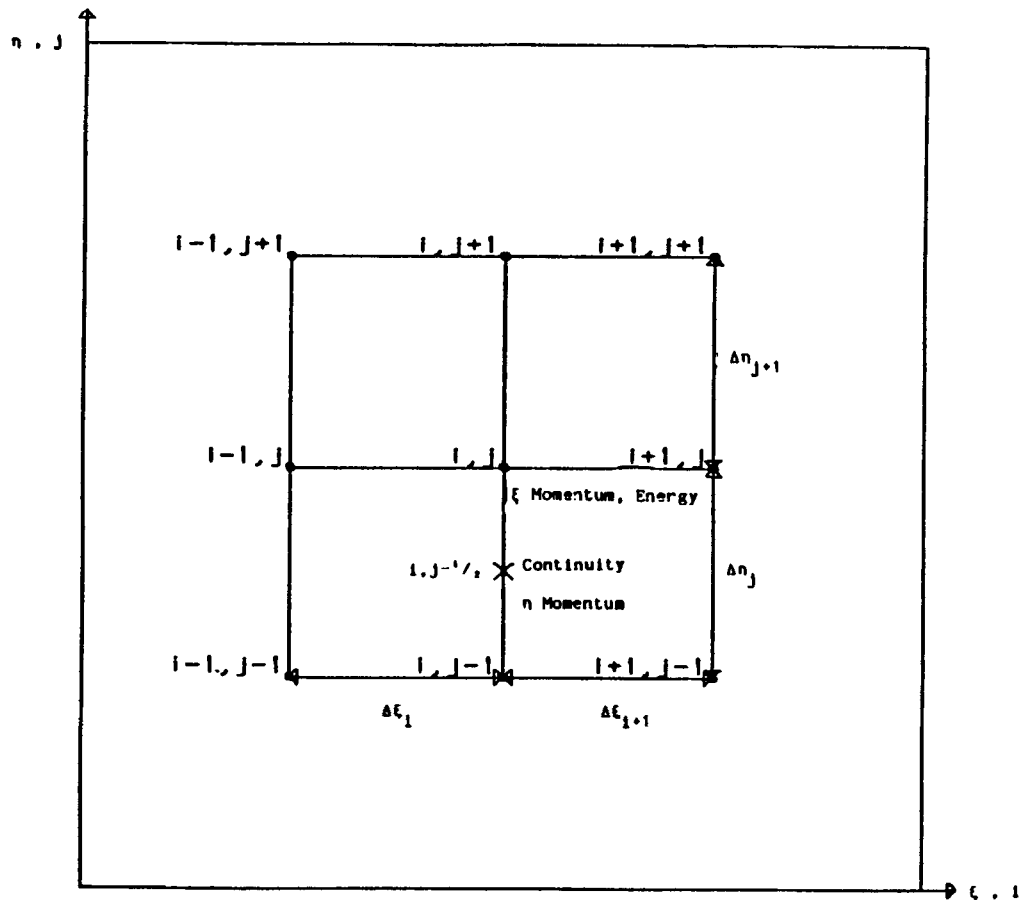

FINITE DIFFERENCE MOLECULE

Figure 1. Illustration of differencing scheme

where

$$K \triangleq \frac{\mathrm{d}p_{\mathrm{fd}}}{\mathrm{d}x} = \left.\frac{\mathrm{d}p_{\mathrm{fd}}}{\mathrm{d}\phi}\right|_{\phi = x = +\infty} = \text{constant} \tag{21}$$

and K is computed and stored before the global relaxation process is started. For each local (quasi-linearization) iteration the value p_{uw,ξ_i} in the ξ-momentum equation source term is adjusted by a Newton method iteration until the $v = 0$ upper wall boundary condition is satisfied.

For the compressible code the differencing was the same as that for the incompressible code, except that the 'node point' equations (ξ-momentum, energy—see Figure 1) were written by averaging derivatives and other quantities about the half-points above and below each node point.[23]

For the compressible code a matrix Thomas algorithm (LU decomposition) is applied. The matrix of equations at the marching station ξ_i retains its block tridiagonal structure for compressible flow, but the matrix row positions of the η-momentum and continuity equations at the half-point below the top wall must be reversed to avoid a zero pivot element on the diagonal.[24,25] With the matrix Thomas algorithm, iteration on $p_{\mathrm{uw},\xi_i}/v_{\mathrm{uw}_i}$ is no longer required.

The trapezoidal-rule differencing exactly provides the correct number of equations so that all boundary conditions on velocity can be satisfied without introducing the wall pressure (see Reference 25, Appendix C).

STABILITY AND CONVERGENCE

During the development of the RNS global pressure relaxation procedure for internal flow, a number of stability and convergence problems were encountered. The first of these, mentioned previously, was a spatial oscillation of the streamwise pressure gradient p_ξ that appeared in each marching sweep. This was relieved by overrelaxation of the p_η term in the η-momentum equation.

The second source of instability was the occurrence of spikes in the global pressure residual field $\Delta p_{i,j}$ ($\Delta p'_{i,j}$ for incompressible flow) near discontinuous changes in the streamwise grid stretch factor σ_ξ. This was rectified by providing smooth transitions between σ_ξ changes via a finite series, hyperbolic tangent formulation (see Reference 25, Appendix D).

A third problem was the destabilizing influence of the secondary, explicit $u^{n-1}_{i+1,j}$ relaxation (resulting from upwind differencing) upon the primary $p^{n-1}_{i+1,j}$ iteration for large-Reynolds-number separated flows. As long as the $u^{n-1}_{i+1,j}$ iteration does not significantly affect the $p^{n-1}_{i+1,j}$ iteration (as in low-Re flow where the viscosity is great enough to damp out this effect, or for small bubbles which do not entail many points of explicit $u^{n-1}_{i+1,j}$ relaxation), the pressure field convergence is not significantly degraded. However, when Re is large and the recirculation substantial, the global pressure relaxation procedure fails. This problem is alleviated by limiting the transients, either by proceeding from a smaller bubble to a larger one through stepwise variation of Re or stepwise increases in the severity of the geometry during the iteration process, or by applying an overrelaxation factor to the viscous terms.

For the aerofoil-in-channel configuration studied in the compressible flow cases, the streamline/potential line grid was generated by the Schwarz–Christoffel mapping technique of Davis[26] and Sridhar and Davis[27] using straight line elements (panels). Inaccuracies were incurred by initially using the analytical Schwarz–Christoffel integrated dz/dw (where $z = x + iy$ is the complex position vector in physical space and $w = \phi + i\psi$ is the complex potential) to determine the metric scale factor h near panel endpoints. The metric $h \triangleq |dz/dw|$ is singular at the endpoints and this induces abrupt, singular changes in the scale factor computed on the body. The singular behaviour is eliminated if numerical differentiation of the integrated z-field is used to calculate h, since the novel numerical integration technique devised by Davis[26] removes the singularities in the final integral.

In the linear incompressible von Neumann stability analysis of Reference 12 it was shown that the largest eigenvalue of the Fourier global amplification matrix is bounded above by

$$|\lambda_{\max}| = 1 - \frac{\pi^2}{2}\left(\frac{\Delta x}{y_m}\right)^2\left(\frac{X_m}{y_m}\right)^2 \approx 1 - \frac{\pi^2}{2}\left(\frac{\Delta \xi}{\eta_m}\right)^2\left(\frac{\xi_m}{\eta_m}\right)^2.$$

This equation demonstrates that although the global relaxation is unconditionally stable, i.e. $|\lambda_{\max}|$ always remains less than one, the maximum eigenvalue does approach one as the ratio $(\Delta\xi/\eta_m) \to 0$. This means that the convergence rate declines as we refine the grid in the ξ-direction and becomes very slow for fine grids. Therefore one must use care in selecting the $\Delta\xi_i$ spacing of the finite difference grid in order to balance the need for adequate resolution against the penalty in convergence rate. Also, refining $\Delta\xi_i$ reduces the artificial viscosity inherent in the upwind differencing of the convection terms and this decreases the damping in the relaxation process. These two effects lead to convergence oscillations for fine meshes and reduce the convergence rate.

As shown in Reference 18, the positive flux component of the p_ξ term also dimishes the artificial viscosity of the discrete approximation. Experimentally it is found that the inherent damping also decreases for increasing Mach number and the resulting oscillations also slow the convergence rate. This effect can be mollified with the use of the σ_v elliptic damping factor; however, this also leads to numerical smearing of the high-gradient regions.

RESULTS

Incompressible channel flow

Incompressible rectangular channel computations were obtained for Reynolds numbers ($Re_{h/2}$) of 10, 75, 100 and 1000 based on the half-channel height. As discussed previously, an initial entry flow region is defined for $\zeta \leq 0{\cdot}2$. It is here that a characteristic 'double-peaked' u-velocity profile is observed experimentally. This behaviour is captured by Navier–Stokes and asymptotic[20] solutions for the channel entry flow, but not with simple boundary layer approximations. The overshoot behaviour is accurately captured with the RNS model. Figure 2 illustrates the solution for $Re_{h/2} = 75$. The peaks are in good agreement with the Navier–Stokes solution of McDonald *et al.*[28] and the RNS solution of Chilukuri and Pletcher[29] obtained with a different numerical scheme. Similar agreement is seen for the centreline velocity distributions.[25]

The incompressible curved channel tests included three geometries of varying constrictions at a Reynolds number $Re_h = 100$ based on maximum channel width, two geometries at $Re_h = 1000$

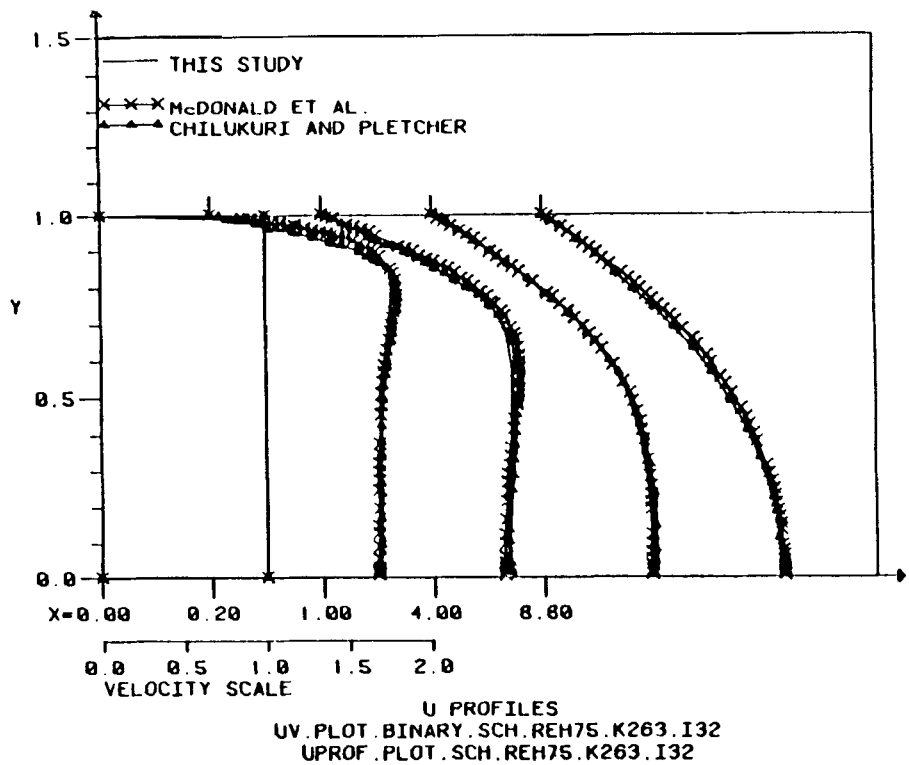

Figure 2. u-profiles, straight half-channel, $Re_{h/2} = 75$, comparison with other RNS and NS solutions

and one geometry at $Re_h = 3000$. The channel walls are selected from two streamlines of the flow over a circular cylinder given by the complex potential

$$w = \phi + i\psi = z + a^2/z, \tag{22}$$

where a is the cylinder radius. The channel was defined by selecting two streamlines a unit distance apart for $x \to -\infty$.[30] The channel minimum thickness at the crest of the cylinder is H; see Figure 3. The lower of the streamlines is a distance y_0 above the centre of the cylinder, which is located at the origin.

The $Re_h = 100$ computations are included for comparison with those given in Reference 21 where full and 'parabolized' Navier–Stokes solutions were obtained with the same Navier–Stokes solver. The differences between the full and approximate Navier–Stokes results were shown to be negligible for these cases. The channels of Reference 21 were also generated by selecting two streamlines a unit distance apart but at some finite location $x = -x_0$. Hence these are very slightly different from those considered herein where $x_0 \to \infty$. Despite the small difference in channel shape, the results are quite similar (see Figure 3 which compares with Case II of Reference 21). A small disparity in bubble size can be attributed to the quasi-conservation scheme of Reference 21. The present RNS scheme conserves mass exactly. As the size of the bubble increases, and consequently the entrained mass flux increases, the disparity in bubble size decreases. The effect of the mass flux error is reduced since it represents a smaller percentage of the entrained mass. It is significant to note that even small changes in entrained mass flux will move the reattachment point considerably. For $Re_h = 100$ and $a^2 = 0.725$, Figure 4 illustrates the associated velocity profiles in the separation region. Figures 5 and 6 depict results for $H = 0.782$, $a^2 = 0.210$ and $Re_h = 1000$. Comparisons are given with the Navier–Stokes solution of Reference 30. For $Re_h = 1000$ it was found that a much finer grid was required. For this calculation (236 × 101) mesh points were specified in order to achieve adequate resolution. The recirculation bubble is quite large and in excellent agreement with the results of Reference 30; see Figures 5 and 6. Slight differences are attributed to the coarser mesh used for the NS calculations in Reference 30. Convergence of the present procedure to a local error of 10^{-6} required 300 global iterations.

Compressible flow: NACA0012 aerofoil in wind tunnel

For the NACA0012 aerofoil-in-wind-tunnel configuration three groups of comparasions are presented. The first series discusses variation of the reference (inlet) Mach number M_r from 0·01 to

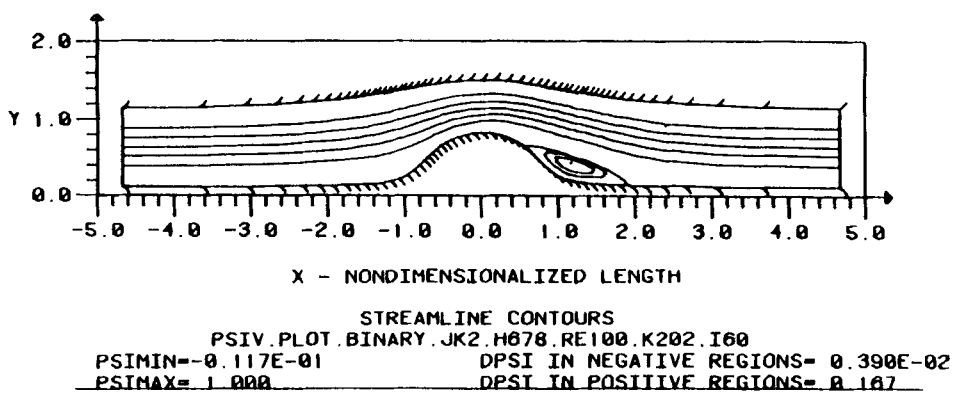

Figure 3. Streamline contours, Joukowski channel, $a^2 = 0{\cdot}585$, $H = 0{\cdot}678$, $Re_h = 100$

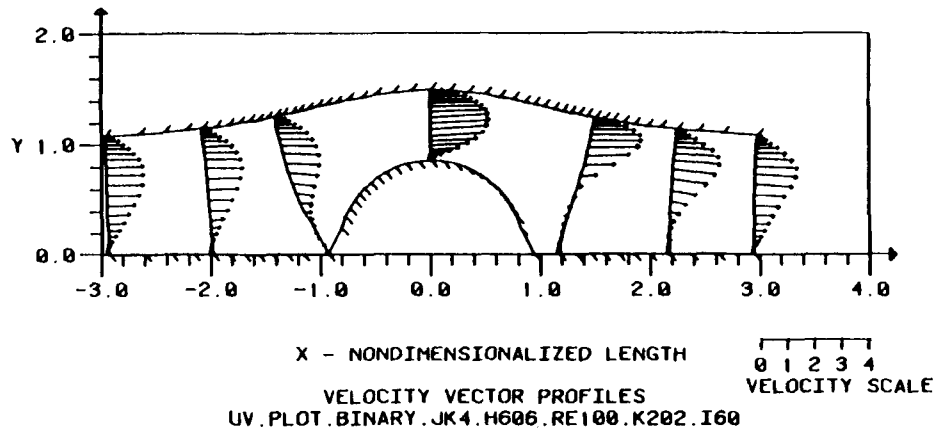

Figure 4. Velocity vector profiles, Joukowski channel, $a^2 = 0{\cdot}725$, $H_{\text{actual}} = 0{\cdot}636$, $Re_h = 100$

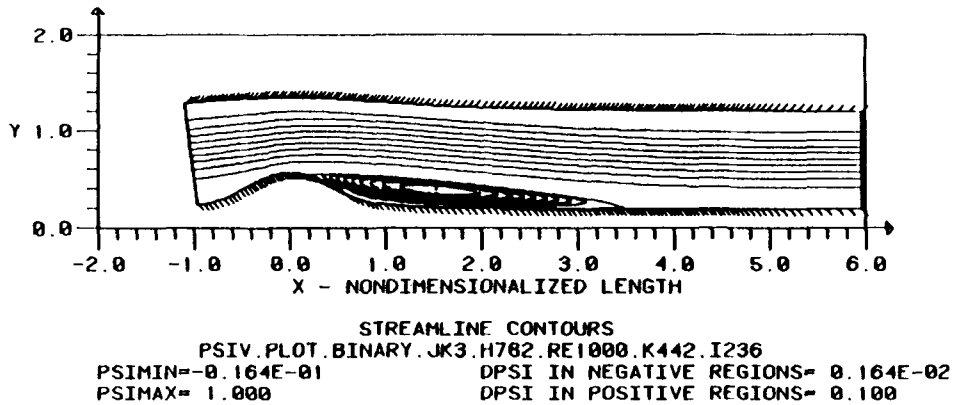

Figure 5. Streamline contours, Joukowski channel, $a^2 = 0{\cdot}210$, $H = 0{\cdot}782$, $Re_h = 1000$

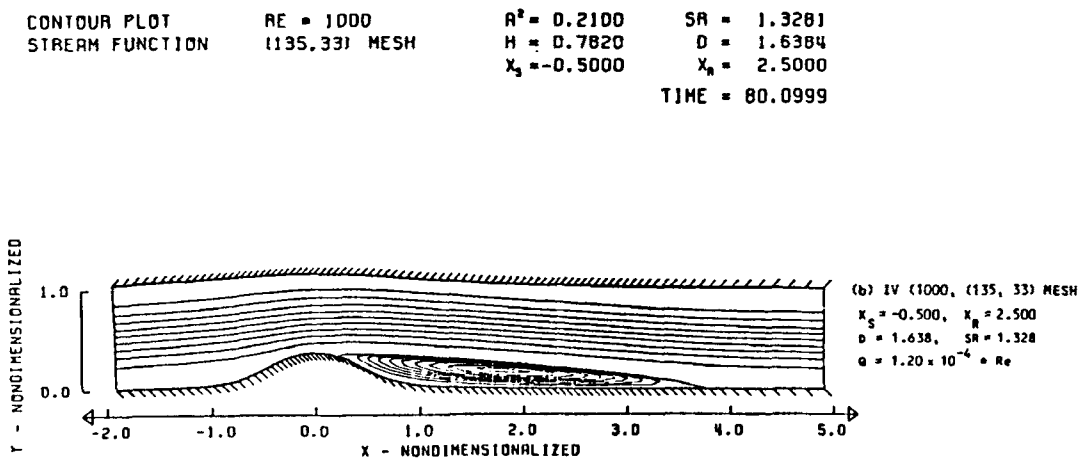

Figure 6. Streamline contours, Joukowski channel, $a^2 = 0{\cdot}210$, $H = 0{\cdot}782$, $Re_h = 1000$. From Reference 25

0·5. These calculations are for fixed reference Reynolds number $Re_L = 1000$ based on aerofoil chord length, and for fixed channel half-height HT = 1·0. The second series considers variation of Re_L from 1000 to 15 000 for fixed $M_r = 0.4$ and fixed HT = 1·0. The third series re-examines the preceding cases but for HT = 2·0. The number of grid points in the x (IMAX) and y (JMAX) directions as well as the total number of iterations (ITER3T) for convergence to 10^{-6} are given in Figures 7–15. Figure 7 depicts a typical grid for $Re_L = 1000$, $M_r = 0{\cdot}01$ and HT = 1·0; every third gridline in ξ and η is displayed.

Figure 8 depicts the typical axial variation of the u-component of velocity for a nearly incompressible case at $M_r = 0{\cdot}01$. The closing of the downstream wake occurs at about 18 chord lengths downstream of the aerofoil. The behaviour near the leading edge is basically inviscid and does not change significantly as Re_L is increased. The distance to wake closure, however, increases significantly as Re_L and M_r are increased.[25]

For $M_r = 0{\cdot}5$ the wake extends the entire downstream length of the grid—some 30 chord lengths; see Figure 9. For $M_r = 0{\cdot}01$ the M-level increases minimally and accelerates towards unity, as would be expected from simple frictional flow analysis, near the end of the duct. For $M_r = 0{\cdot}5$ the Mach number acceleration was significant. The Mach number was 0·859 at the exit station and the peak Mach number was 0·918 64. This occurred in the aerofoil section of the duct.

Table I tabulates the ratio $\Delta p^*/p_r = \gamma_r M_r^2 p_{\text{inlet}}$ of actual pressure drop across the length of the duct to exit pressure p_r, as well as the ratio of pressure drop in each channel to the base quasi-incompressible flow case at $M_r = 0{\cdot}01$. Also tabulated for each M_r is the dimensionless mass flux m, centreline exit Mach number $M_{i\max}$, average exit pressure gradient $p_{\xi i\max}$ and exit friction coefficient $C_{f i\max}$.

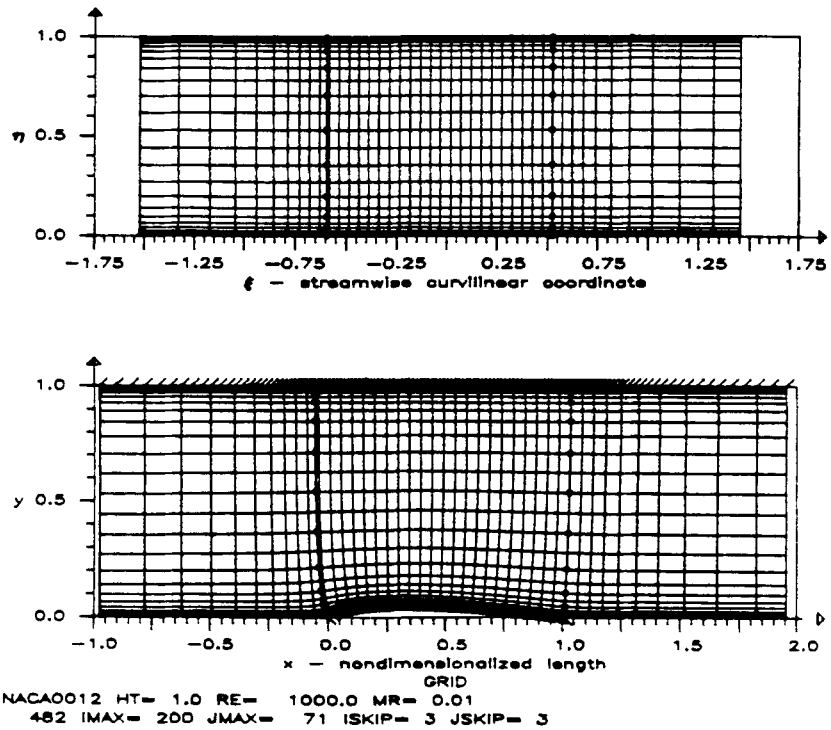

Figure 7. Grid for NACA0012 aerofoil in wind tunnel, HT = 1·0, $Re_L = 1000$, $M_r = 0{\cdot}01$, IMAX = 200, JMAX = 71

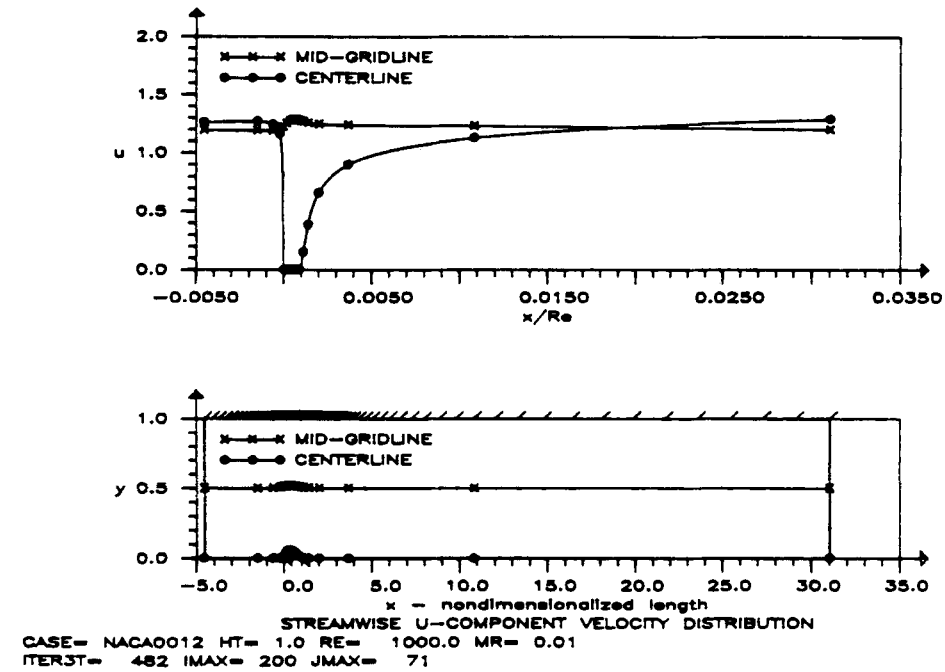

Figure 8. Streamwise u-distributions, NACA0012 aerofoil in wind tunnel, HT = 1·0, $Re_L = 1000$, $M_r = 0{\cdot}01$

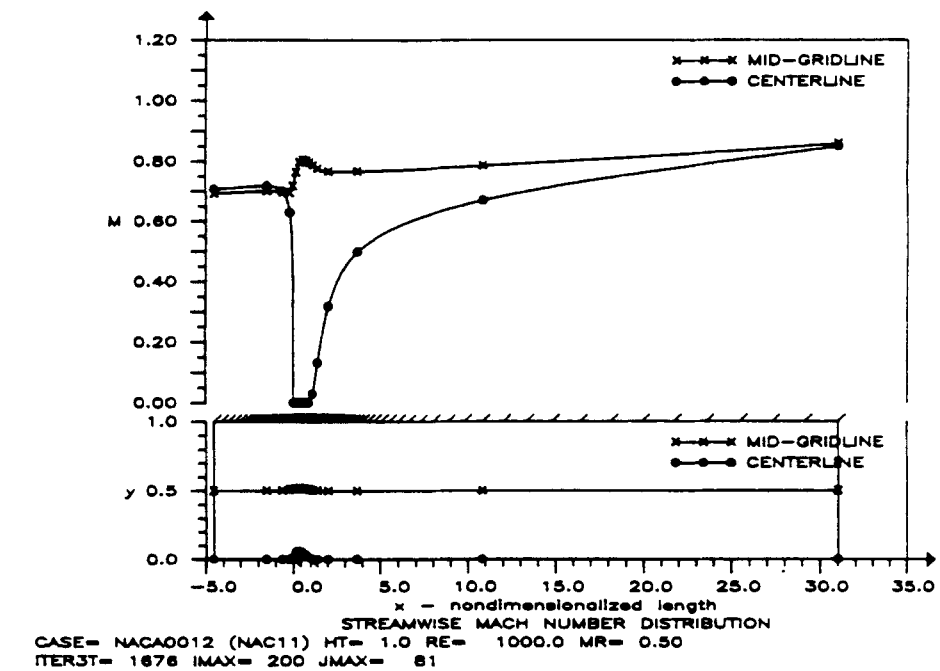

Figure 9. Streamwise Mach number distributions, NACA0012 aerofoil in wind tunnel, HT = 1·0, $Re_L = 1000$, $M_r = 0{\cdot}50$

The pressure drop, mass flux and exit Mach number all increase non-linearly with M_r, as expected from simple frictional flow. For the lower-Mach-number cases, $p_{\xi_{imax}}$ and $C_{f_{imax}}$ are close to the theoretical fully developed values $p_{fd,\xi} = -3/Re$ and $C_f = 6/Re$.

Typical streamline contour plots (Figures 10 and 11) illustrate the growth of the aerofoil separation bubble with increasing Re_L. There is a pronounced drop in induced mass flow rate m resulting from the diminished viscous pressure drop at larger Re_L; see Table II.

From a comparison of streamwise pressure distributions at $Re_L = 1000$ and 5000 in Figures 12 and 13, we observe the large drop in peak pressure on the aerofoil from $Re_L = 1000$ to $Re_L = 5000$ that we would expect from reduced viscosity and consequent decreased viscous pressure drop. From $Re_L = 5000$ to 15000 there is little influence of the Reynolds number change. Many additional results are given in Reference 25.

As presented in Reference 20, the relevant viscous parameter for rectangular channel flow is the Reynolds number based on channel half-height $Re_{h/2}$. For our HT = 1·0 cases $Re_{h/2} = Re_L$.

Table I. Comparison of cases for varying M_r, fixed $Re_L = 1000$, fixed exit pressure p_r and HT = 1·0

M_r	$\Delta\bar{p}^*/p_r$	$\Delta\bar{p}^*(M_r)/\Delta\bar{p}^*(0{\cdot}01)$	m	M_{imax}	$p_{\xi_{imax}}$	$C_{f_{imax}}$
0·01	$7{\cdot}9219 \times 10^{-5}$	1·0	1·99848	0·0127	− 0·00439	0·0072211
0·10	0·0080938	102·17	2·01453	0·130	− 0·00452	0·0073089
0·20	0·034669	437·64	2·06773	0·260	− 0·00493	0·0076024
0·30	0·088666	1119·25	2·17581	0·415	− 0·00585	0·0082126
0·40	0·19705	2487·39	2·39267	0·585	− 0·00812	0·0095147
0·50[a]	0·50087	6322·61	3·00238	0·859	− 0·01916	0·014072
0·50[b]	0·48908	6173·72	2·97876	0·8527	− 0·01871	0·013893

[a] $\sigma_v = 0{\cdot}8$. [b] $\sigma_v = 1{\cdot}0$.

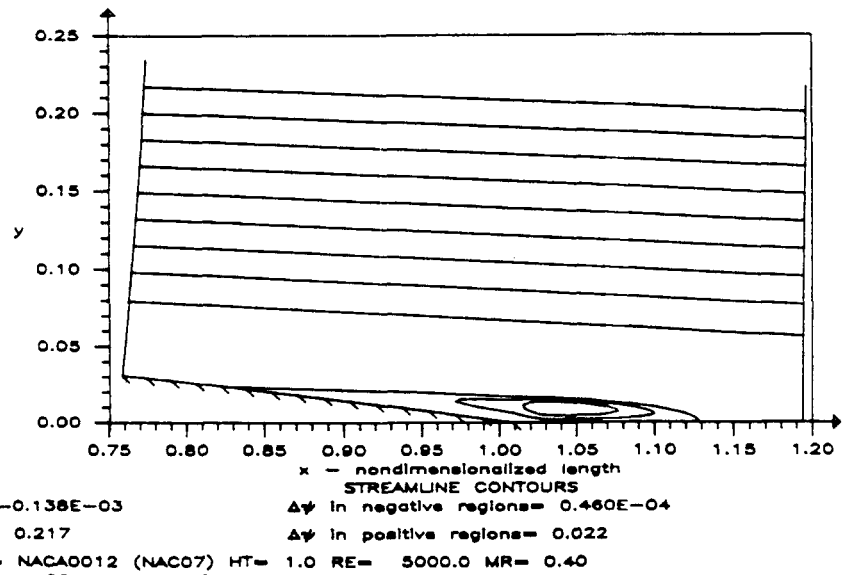

Figure 10. Streamline contours, NACA0012 aerofoil in wind tunnel, HT = 1·0, $Re_L = 5000$, $M_r = 0{\cdot}40$

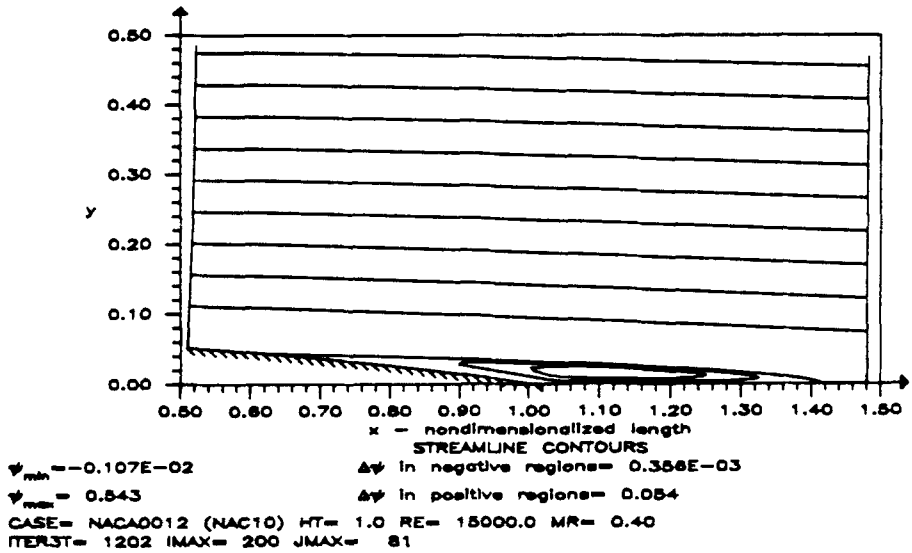

Figure 11. Streamline contours, NACA0012 aerofoil in wind tunnel, HT = 1·0, $Re_L = 15000$, $M_r = 0{\cdot}40$

Table II. Comparison of cases for varying Re, fixed $M_r = 0{\cdot}4$, fixed exit pressure p_r and HT = 1·0

Re_L	$Re_{h/2}$	$\Delta p^*/p_r$	$\Delta p(Re)/\Delta p^*(1000)$	m	$M_{i\max}$	$C_{f_{\max}}$	$C_{f_{i\max}}$
1000	1000	0·19705	1·0	2·39267	0·56758	0·37524	0·0095147
5000	5000	0·07239	0·36737	2·14467	0·50394	0·14520	0·0023641
10000	10000	0·04930	0·25017	2·09842	0·47527	0·091705	0·0014122
15000	15000	0·03963	0·20112	2·07905	0·46187	0·070012	0·0010623

Furthermore, from Reference 20 we see that the applicable functional forms of $Re_{h/2}$ for use in perturbation series are $Re_{h/2}^{-1/2}$ in the initial portion of the entry flow region and $Re_{h/2}^{-1}$ thereafter. These indicate an inverse dependence of flow behaviour on $Re_{h/2}$. The peak C_f on the aerofoil[25] indicates this inverse trend with Re. The ratios of successive peak C_f values, $C_f(Re_2)_{\max}/C_f(Re_1)_{\max}$, are such that

$$\frac{Re_1}{Re_2} < \frac{C_f(Re_2)_{\max}}{C_f(Re_1)_{\max}} < \sqrt{\left(\frac{Re_1}{Re_2}\right)}.$$

The decreasing rate of velocity and Mach number acceleration for increasing Re is seen most clearly by comparing the exit Mach numbers $M_{i\max}$. Comparisons of these and other flow quantities with increasing Re are given in Table II.

The Re_L parameters for the HT = 2·0 cases are identical to their HT = 1·0 counterparts, although the channel development parameter $Re_{h/2}$ is now double that of the HT = 1·0 cases. Thus we would expect that those quantities that depend primarily on the channel flow development (C_f on wind tunnel walls) should scale with $Re_{h/2}$. This assumption is confirmed by comparison of the mass flow rates for $Re_L = 1000$. The value of $\frac{1}{2}m$ for the HT = 2·0 case is less than m for the corresponding HT = 1·0 case, although the channel height has been doubled. These and other flow quantities are tabulated for increasing Re for the HT = 2·0 cases in Table III.

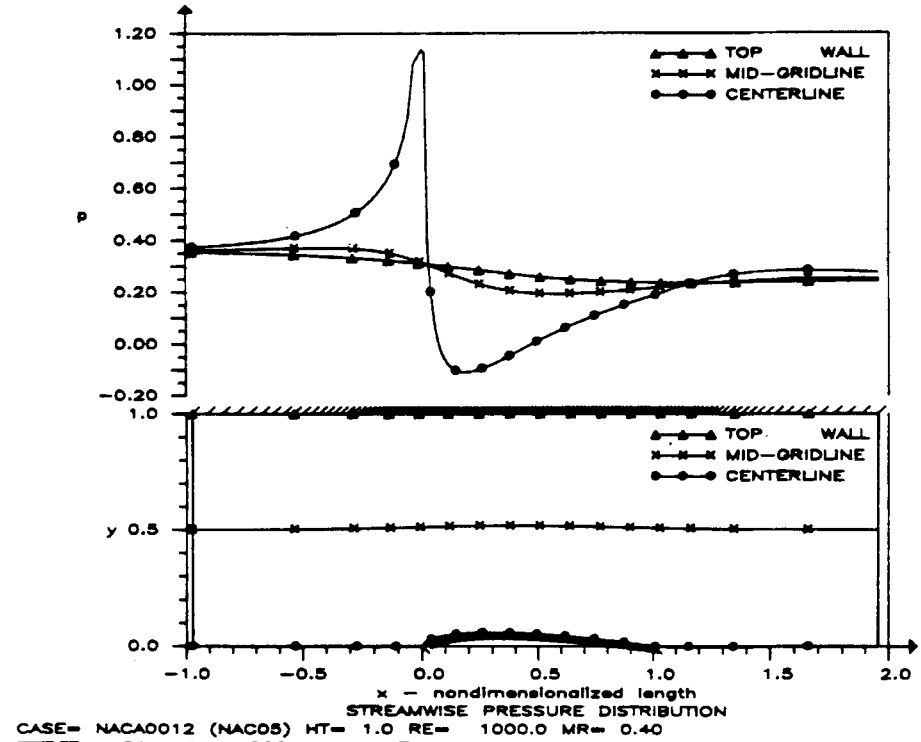

Figure 12. Streamwise pressure distributions, NACA0012 aerofoil in wind tunnel, HT = 1·0, $Re_L = 1000$, $M_r = 0{\cdot}40$

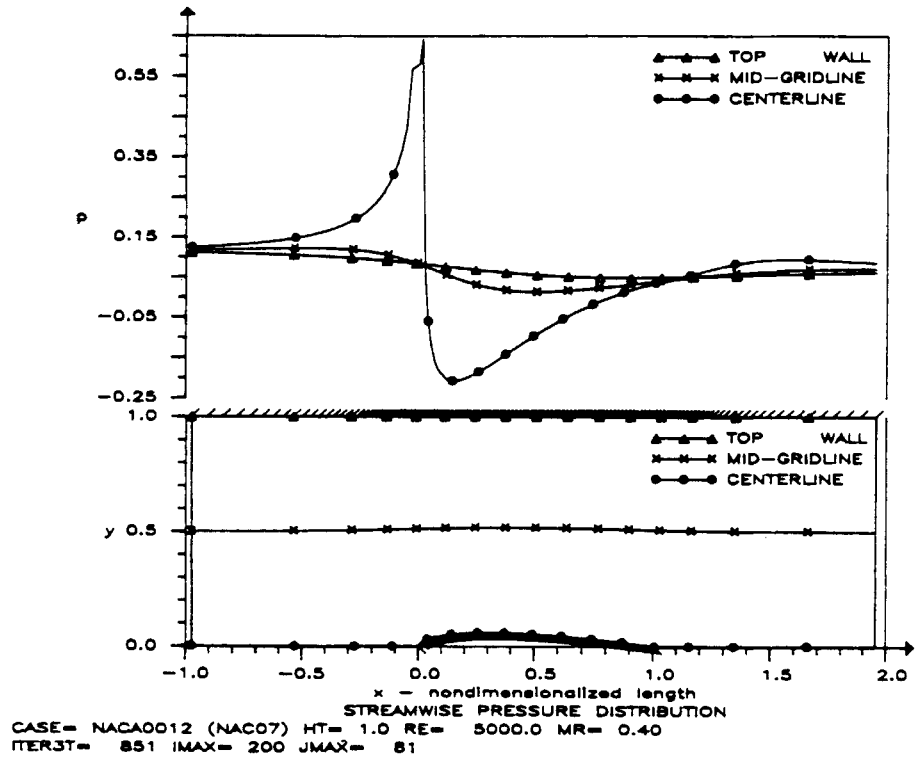

Figure 13. Streamwise pressure distributions, NACA0012 aerofoil in wind tunnel, HT = 1·0, $Re_L = 5000$, $M_r = 0{\cdot}40$

A comparison of the corresponding recirculating flow streamlines of these two case sets[25] reveals that the corresponding bubbles are almost identical. This indicates that the local aerofoil flow is relatively insensitive to the wall location even for HT = 1·0. The streamwise pressure distributions and pressure drop ratios $\Delta p^*/p_r$ (compared in Tables II and III) demonstrate that the pressure levels for HT = 1·0 are correspondingly higher than those for HT = 2·0. This is consistent with the notion that the channel flow properties, e.g. pressure drop, scale with $Re_{h/2}$ rather than Re_L. By similar reasoning we can anticipate the larger-Mach-number acceleration of the narrower channel as reflected by the larger values of M_{imax}.

Figure 14 illustrates the rather unusual mode of convergence exhibited by the compressible flow cases. The maximum pressure residual $\Delta p \triangleq \max_{i,j} |p^n_{i,j} - p^{n-1}_{i,j}|$ travels upstream as a wave of

Table III. Comparison of cases for varying Re, fixed $M_r = 0{\cdot}4$, fixed exit pressure p_r and HT = 2·0

Re_L	$Re_{h/2}$	$\Delta p^*/p_r$	$\Delta p(Re)/\Delta p^*(1000)$	m	M_{imax}	$C_{f_{max}}$	$C_{f_{imax}}$
1000	2000	0·08178	1·0	4·32884	0·51337	0·34608	0·0056345
5000	10000	0·03380	0·41334	4·13578	0·45335	0·12911	0·0017501
10000	20000	0·02354	0·28787	4·09448	0·43812	0·083833	0·0011156
15000	30000	0·01909	0·23347	4·07657	0·43135	0·064778	0·00086695

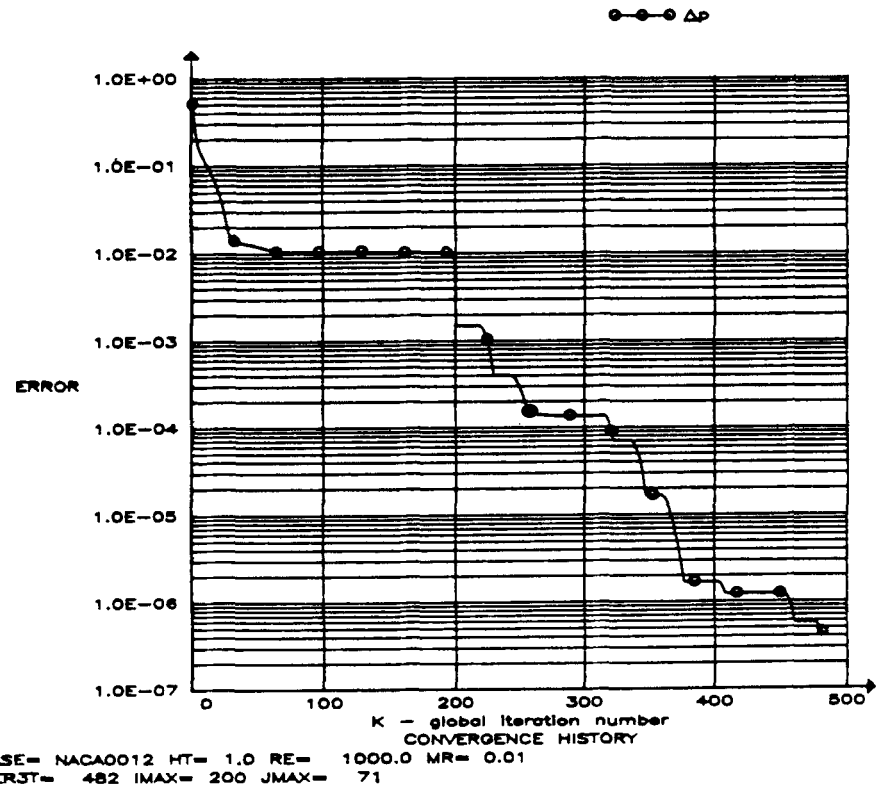

Figure 14. Convergence history, NACA0012 aerofoil in wind tunnel, HT = 1·0, $Re_L = 1000$, $M_r = 0{\cdot}01$

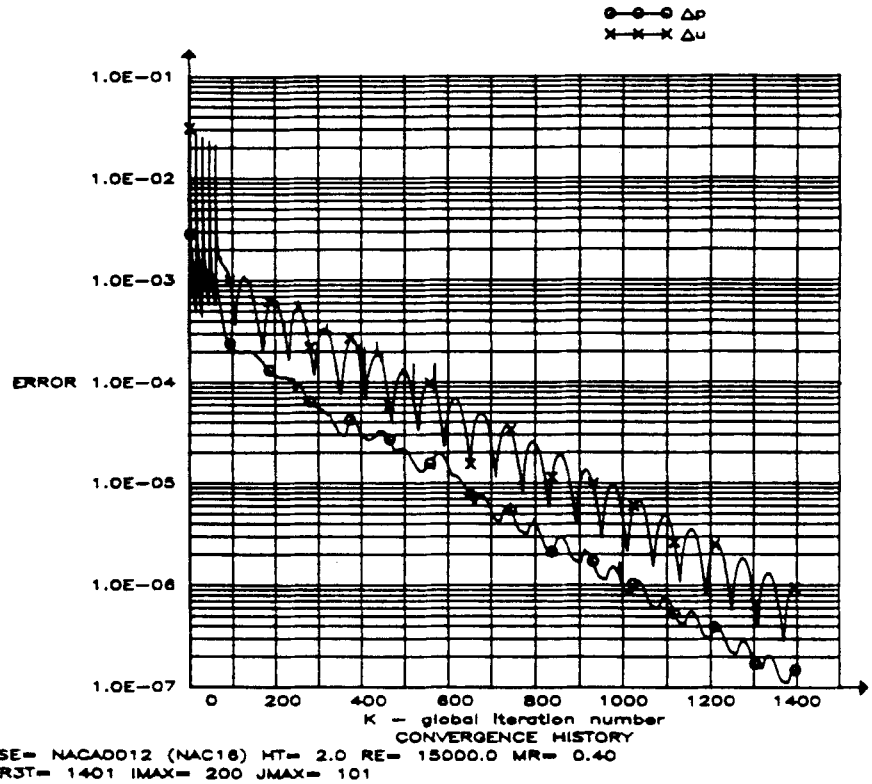

Figure 15. Convergence history, NACA0012 aerofoil in wind tunnel, HT = 2·0, $Re_L = 15000$, $M_r = 0{\cdot}40$

almost constant amplitude until it reaches the inlet station. The mass flux adjusts to the pressure information and consequently there is a pronounced drop in the Δp error level in the grid. Subsequent Δp waves of smaller amplitude travel upstream and the process is repeated. The convergence rate systematically decreases for increasing M_r.[25] A multigrid method recently applied for RNS external flow by Himansu and Rubin[31] has accelerated convergence by an order of magnitude. This is suggested for internal flows as well.

The Reynolds number variation for HT = 2·0 exhibits similar but elevated convergence history curves. A tendency towards increasing Δu residuals was evidenced for the wider channel. By $Re_L = 15000$ (Figure 15) the Δp variation had changed to a damped oscillation in phase with Δu. The spikes observed for the first 80 iterations in Figure 15 are simply a result of the normal relaxation initialization process involving stepwise increases in Re_L. Engineering accuracy is achieved in 200–300 iterations. Once again, multigrid acceleration should reduce this by an order of magnitude.

CONCLUSIONS

The global pressure flux-split relaxation procedure developed by Rubin and co-workers for the solution of the RNS equations in external flow has been extended here to the internal flow problem.

The internal flow application introduces the consideration of mass flux conservation and evaluation. The mass conservation constraint introduces a greater degree of stiffness in the RNS

system. This gives rise to non-physical oscillations which are suppressed by modifying the pressure relaxation in the normal momentum equation. The iterative variation of the inlet mass flux leads to a step-like convergence rate reflecting the interaction of pressure waves with the inlet boundary condition. Although these features complicate the application of the method to internal flow, it is nervertheless stable and capable of calculating flows with strong viscous–inviscid interaction and large recirculation regions for large Reynolds number.

The present study was directed towards the stable adaptation of the RNS solution procedure to internal flow and the evaluation of flows with large recirculation and blunt leading edge geometries. These aims have been accomplished. Future work will examine convergence enhancement and the effectiveness of the multigrid method.

ACKNOWLEDGEMENT

This research was supported by NASA Grant NAG 3-397 LE.

REFERENCES

1. H. Schlichting, *Boundary Layer Theory*, McGraw-Hill, New York, 1968.
2. M. Van Dyke, *Perturbation Methods in Fluid Mechanics*, The Parabolic Press, Stanford, 1978.
3. A. P. Rothmayer, 'A study of high Reynolds number laminear separation', *Ph.D. Dissertation*, Deptment of Aerospace Engineering and Engineering Mechanics, University of Cincinnati, May 1985.
4. K. Stewartson, 'Multistructured boundary layers on flat plates and related bodies', *Adv. Appl. Mech.*, **14**, 145–239 (1974).
5. S. Rudman and S. G. Rubin, 'Hypersonic viscous flow over slender bodies wth sharp leading edges', *AIAA. J.*, **6**, 1883–1890 (1968).
6. S. G. Rubin and T. C. Lin, 'Numerical methods for two and three-dimensional viscous flow problems: application to hypersonic leading edge equations', *J. Comput. Phys.*, **9**, 339–364 (1972).
7. Y. C. Vigneron, J. V. Rakich and J. C. Tannehill, 'Calculation of supersonic viscous flow over delta wings with sharp subsonic leading edges', *AIAA Paper 78-1137*, Seattle, WA, July 1978.
8. S. G. Rubin, 'RNS pressure relaxation and flux vector splitting', *Comput. Fluids*, **16**, 485–490 (1988).
9. S. G. Rubin and A. Lin, 'Marching with the parabolized Navier–Stokes equations', *Israel J. Technol.*, **18**, 21–31 (1980).
10. A. Lin and S. G. Rubin, 'Three-dimensional supersonic viscous flow over a cone at incidence', *AIAA J.*, **20**, 1500–1507 (1982).
11. S. G. Rubin and D. R. Reddy, 'Analysis of global pressure relaxation for flows with strong interaction and separation', *Comput. Fluids*, **11**, 281–306 (1983).
12. D. R. Reddy, 'Global pressure relaxation procedure for laminar and turbulent incompressible flows with strong interaction and separation', *Ph.D. Dissertation*, Department of Aerospace Engineering and Applied Mechanics, University of Cincinnati, March 1983.
13. P. K. Khosla and H. T. Lai, 'Global PNS solutions for subsonic strong interaction flow over a cone–cylinder–boattail configuration', *Comput. Fluids*, **11**, 325–339 (1983).
14. H. T. Lai, 'Global PNS solutions for subsonic strong interaction flows', *M.S. Thesis*, Department of Aerospace Engineering and Applied Mechanics, University of Cincinnati, December 1982.
15. D. R. Reddy and S. G. Rubin, 'Subsonic/transonic, viscous/inviscid relaxation procedures for strong pressure interactions', *AIAA Paper 84-1627*, Snowmass, CO, June 1984.
16. H. T. Lai and P. K. Khosla, 'A global relaxation procedure for inviscid as well as for viscous transonic strong interaction flows', *Int. Symp. on Computational Fluid Dynamics*, Tokyo, 1985, pp. 166–176.
17. M. Barnett, 'Solution of the parabolized Navier–Stokes equations for supersonic flows by fully implicit method with an analysis of departure solution behavior', *M.S. Thesis*, Department of Aerospace Engineering and Applied Mechanics, University of Cincinnati, August 1981.
18. H. T. Lai, 'Global pressure relaxation procedure with application to viscous and inviscid flows', *Ph.D. Dissertation*, Department of Aerospace Engineering and Engineering Mechanics, University of Cincinnati, November 1985.
19. S. V. Ramakrishnan and S. G. Rubin, 'Global pressure relaxation for steady, compressible, laminar, 2-dimensional flows with full pressure coupling and shock waves', *Report No. AFL-84-100*, Department of Aerospace Engineering and Applied Mechanics, University of Cincinnati, July 1984.
20. S. G. Rubin, P. K. Khosla and S. Saari, 'Laminar flow in rectangular channels. Part I: Entry analysis. Part II: Numerical solution for a square channel', *Comput. Fluids*, **5**, 151–173 (1977).
21. U. Ghia, K. N. Ghia, S. G. Rubin and P. K. Khosla, 'Study of incompressible flow separation using primitive variables', *Comput. Fluids*, **9**, 123–142 (1981).

22. R. Ramamurti, 'A semi-elliptic analysis and hybrid C–H grids for two-dimensional viscous flows through cascades', *Ph.D. Dissertation*, Department of Aerospace Engineering and Engineering Mechanics, University of Cincinnati, June 1986.
23. M. Barnett, 'The calculation of supersonic flows with strong viscous–inviscid interaction using the parabolized Navier–Stokes equations', *Ph.D. Dissertation*, Department of Aerospace Engineering and Applied Mechanics, University of Cincinnati, May 1984.
24. D. R. Reddy and S. G. Rubin, 'Consistent boundary conditions for reduced Navier–Stokes (RNS) scheme applied to three-dimensional viscous flows', *ASME J. Fluids Eng.*, **10,** 306–314 (1988).
25. D. Rosenbaum, 'Global pressure relaxation procedure for solution of laminar, 2-dimensional reduced Navier–Stokes equations for internal flow', *Ph.D. Dissertation*, Department of Aerospace Engineering and Engineering Mechanics, University of Cincinnati, June 1988.
26. R. T. Davis, 'Numerical methods for coordinate generation based on Schwarz–Christoffel transformations', *AIAA Paper 79-1463, 4th Computational Fluid Dynamics Conf.*, July 1979.
27. K. P. Sridhar and R. T. Davis, 'A Schwarz–Christoffel method for generating internal flow grids', *Proc. Winter Ann. Meeting, ASME*, Washington DC, 15–20 November 1981, pp. 35–44.
28. J. W. McDonald, V. E. Denny and A. F. Mills, 'Numerical solutions of the Navier–Stokes equations in inlet regions', *ASME J. Appl. Mech.*, **39,** Ser. E, 873–878 (1972).
29. R. Chilukuri and R. H. Pletcher, 'Numerical solutions to the partially parabolized Navier–Stokes equations for developing flow in a channel', *Numer. Heat Transfer*, **3,** 169–188 (1988).
30. G. A. Osswald, 'A direct numerical method for the solution of unsteady Navier–Stokes equations in generalized orthogonal coordinates', *Ph.D. Dissertation*, Department of Aerospace Engineering and Applied Mechanics, University of Cincinnati, December 1983.
31. A. Himansu and S. G. Rubin, 'Multigrid acceleration of a relaxation procedure for the RNS equations', *AIAA J.*, **26**(9), 1044–1051 (September 1988).